

A numerical model for full and partial penetration hybrid laser welding of thick-section steels

Kalkhorani, Farhang Farrokhi; Endelt, Benny Ørtoft; Kristiansen, Morten

Published in:
Optics & Laser Technology

DOI (link to publication from Publisher):
[10.1016/j.optlastec.2018.08.059](https://doi.org/10.1016/j.optlastec.2018.08.059)

Creative Commons License
CC BY-NC-ND 4.0

Publication date:
2019

Document Version
Publisher's PDF, also known as Version of record

[Link to publication from Aalborg University](#)

Citation for published version (APA):
Kalkhorani, F. F., Endelt, B. Ø., & Kristiansen, M. (2019). A numerical model for full and partial penetration hybrid laser welding of thick-section steels. *Optics & Laser Technology*, 111, 671-686.
<https://doi.org/10.1016/j.optlastec.2018.08.059>

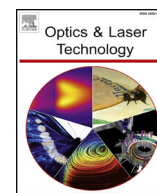
General rights

Copyright and moral rights for the publications made accessible in the public portal are retained by the authors and/or other copyright owners and it is a condition of accessing publications that users recognise and abide by the legal requirements associated with these rights.

- Users may download and print one copy of any publication from the public portal for the purpose of private study or research.
- You may not further distribute the material or use it for any profit-making activity or commercial gain
- You may freely distribute the URL identifying the publication in the public portal -

Take down policy

If you believe that this document breaches copyright please contact us at vbn@aub.aau.dk providing details, and we will remove access to the work immediately and investigate your claim.



Full length article

A numerical model for full and partial penetration hybrid laser welding of thick-section steels

Farhang Farrokhi*, Benny Endelt, Morten Kristiansen

Aalborg University, Department of Materials and Production, Fibigerstraede 16, Aalborg 9220, Denmark

HIGHLIGHTS

- Melt profile was significantly different in full and partial penetration welding.
- A numerical model was presented and validated for the experiments.
- A *double-conical* boundary condition allowed modeling the *hourglass shape* welds.
- The model can potentially be used for solving engineering problems.

ARTICLE INFO

Keywords:

Finite element
Numerical modeling
Laser welding
Full penetration
Heat source
Double-conical
Residual stress

ABSTRACT

Full and partial penetration welding using high power lasers exhibit different melt pool geometries. The main difference is that full penetration welds tend to widen at the root side. In recent years, full penetration laser welding has been modeled using sophisticated multiphase numerical models. However, less computationally-complex thermo-mechanical models that are capable of accounting for the root widening phenomenon in full penetration laser welding are lacking. In this study, hybrid laser welding was performed for full and partial penetration modes on butt joints of structural steel. A numerical model was presented that used a three-dimensional transient Finite Element (FE) analysis and thermal conduction heat transfer for calculating the temperature fields in both full and partial penetration welding modes. For this purpose, a *double-conical* volumetric heat source was developed based on the three-dimensional conical (TDC) heat source in the literature. The model was validated and calibrated with different experiments. The results show that the model is capable of calculating the transient temperatures for the common melt pool geometries obtainable by the full and partial penetration hybrid laser welding of thick-section steels. The model can potentially be employed as the basis for predicting e.g. microstructural properties or residual stresses for a given welding procedure.

1. Introduction

Hybrid laser welding is a complicated process that involves several complex physical phenomena. With the development of numerical techniques and high power computers, numerical methods seem to be an essential and also convenient way to better understand the underlying mechanisms of the process [1]. In this regard, several studies have been carried out and reported in the literature, and the review of the subject can be found in [1–5].

The modeling of hybrid laser welding is inherently challenging, as it must account for the high temperature gradients and rapid cooling rates due to the high energy intensity of laser beams. In addition, such a process involves several physical mechanisms that are highly coupled, for example, mechanisms of laser-material interaction and absorption,

phase transition, and energy transfer in solid, liquid, and gas phases [6]. Although a few attempts for the relatively comprehensive simulation of laser keyhole welding can be found in the literature (e.g. [7–9]), the simulation of the whole phenomena in the process is not yet possible [2]. However, for both arc and laser welding, the simplified so called “thermo-mechanical” models [2] that are mainly based on thermal conduction heat transfer have been used extensively in the literature, e.g. in [10–18]. These models can be employed for many engineering problems in welding, e.g. for the prediction of the weld pool geometry and the computation of residual stresses without the need to consider multi-physical and fluid flow effects. In such models, the absence of fluid flow, and hence, thermal convection, is assumed to be compensated for by using a volumetric “equivalent” heat source that can be adapted and calibrated with respect to the experimental melt pool

* Corresponding author.

E-mail addresses: ffk@mp.aau.dk (F. Farrokhi), endelt@mp.aau.dk (B. Endelt), morten@mp.aau.dk (M. Kristiansen).<https://doi.org/10.1016/j.optlastec.2018.08.059>

Received 15 April 2018; Received in revised form 16 July 2018; Accepted 31 August 2018

Available online 20 September 2018

0030-3992/ © 2018 The Authors. Published by Elsevier Ltd. This is an open access article under the CC BY-NC-ND license (<http://creativecommons.org/licenses/by-nc-nd/4.0/>).

geometries.

Various volumetric heat sources have been proposed in the literature. For instance, the *double-ellipsoidal* heat source proposed by Goldak et al. [19] has been used extensively in the literature, especially for the arc welding processes. Even though, the heat source was intended to be used for both shallow and deep penetration processes, Goldak and coworkers [20] suggested the use of a conical distribution power density for deep penetration welding. Recently, Flint et al. [21] developed an extended version of the double-ellipsoidal heat source that can be applied to narrow-groove and very deep keyhole weld configurations as well. However, for the deep penetration keyhole welding processes, the *conical* heat source has been one of the most popular and has been implemented in commercial Finite Element (FE) software for many years. Wu et al. [17] proposed a modified *three-dimensional conical* (TDC) heat source. This relatively simple heat source considers a Gaussian heat intensity distribution along the workpieces thickness. Thanks to its semi-cylindrical geometry, the TDC heat source is suitable for modeling deep penetration welding processes such as keyhole plasma arc welding and laser welding. Alternatively, the *cylindrical-involution-normal* (CIN) heat source proposed by Ranatowski [22] can be used for modeling such welding processes. Although it is relatively sophisticated, it offers a high level of flexibility and control to the user to manipulate the heat distribution density along the thickness direction as well as radially. However, the combination of two volumetric heat sources is sometimes required to obtain accurate thermal fields [16,23–25].

Several laser welding experiments have been modeled successfully in the literature using different volumetric heat sources. Nevertheless, these models have been mainly focused on partial penetration welding, and none of them consider the root widening that often appears in the case of full penetration welding. Table 1 summarizes the common weld shapes that are obtained by the hybrid laser welding of thick-section steels. Three types of weld cross section shapes are often seen, depending on the penetration-mode. Partial penetration welds often exhibit a typical *bell shape* cross section consisting of a relatively wide width in the arc-dominated region and a relatively narrow semi-cylindrical shape in the laser-dominated region. Full penetration welds however, are often associated with an *hourglass shape* cross section as a result of a *root widening* phenomenon, which can be minimal or significant depending on the plate thickness and process parameters.

The reason for root widening in full penetration laser welds lies in the characteristics of the melt flow during the process. In the weld pool during laser welding, several complex phenomena result in the circulation of the liquid metal [41]. This melt flow induces a convective heat transfer that has a significant influence on the temperature distribution, and hence, the melt pool geometry [24,42]. Recent studies on laser

welding with solid-state lasers reveal that melt flow is different, depending on the penetration-mode [41,43] (see Fig. 1a). In full penetration laser welding, melt pool at the root side may be longer and more unstable than on the top side [44]. Powell et al. [41] suggest that, during full penetration laser welding, (i) the fact that the root of the weld is insulated on one side by the air and is less effectively cooled by the substrate – together with (ii) the strong downward thrust on the melt in the keyhole – resulting in the extension of the melt at the root, and hence, the root widening of full penetration welds. This has also been reported by Haug et al. [45], where they observed the root flow pattern on the lateral (longitudinal) section of the weld that was associated with an hourglass shape weld at the cross section (see Fig. 1b).

Although full penetration laser and hybrid laser welding have been simulated using relatively sophisticated fluid flow models [44,46], simple thermo-mechanical models that are based on thermal conduction heat transfer are lacking in the literature. A new volumetric heat source model is required for such models, to account for the root widening phenomenon in the full penetration keyhole welding processes.

1.1. Scope and objectives

According to the introduction, this paper primarily attempts to develop a numerical model based on the FE method and thermal conduction heat transfer to account for the root widening phenomenon in the full penetration hybrid laser welding of steel. In addition, it aims at investigating the effect of penetration-mode (for a constant heat input) on the weld geometry of hybrid laser welds. For the entire numerical calculations, the unit system (b) was used according to LS-DYNA manual [47].

1.2. Case studies

Three case studies were considered for the investigation, to account for the common weld cross sections attainable by hybrid laser welding shown in Table 1. These case studies have been depicted on the lateral section in Fig. 2, which is based on a recent work by Frostevarg [48], in which five different regimes for the root topology of laser keyhole welding have been categorized: (i) insufficient penetration or quasi full penetration, (ii) Full penetration with root humping (Fig. 2b), (iii) Full penetration with good results (Fig. 2c), (iv) root sagging, and (v) over penetration.

However, for the sake of simplicity, only three case studies that are depicted in Fig. 2 were defined in this paper as following:

- Case I: Partial penetration (schematic A in Table 1)
- Case II: Full penetration: wide root (schematic B in Table 1)
- Case III: Full penetration: thin root (schematic C in Table 1)

Welding experiments corresponding to Cases I and II were carried out originally in this paper. However, for Case III, the experiments were adopted from the experimental results of an external study [49].

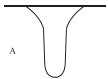
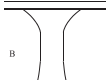
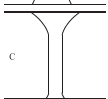
2. Experimental procedure

In this section, the hybrid laser welding procedure for Cases I and II will be described. Experimental procedure for Case III can be found in [49].

In order to obtain full and partial penetration welds, welding was performed to form a butt joint in steel plates. Table 2 presents the welding process parameters. Both full and partial penetration experiments used the same parameters, which were selected for obtaining a 10 mm penetration depth in a single pass. Therefore, using plates with 10 and 25 mm thicknesses allowed the obtaining of full and partial penetration welds, respectively, in which the welding heat input and penetration depth could be roughly identical.

Table 1

Geometrical classification of the common weld cross section shapes obtained by hybrid laser welding of thick-section steels (10 mm and above) based on their penetration-mode. Note: mainly includes solid-state lasers and butt joints of structural steels.

Penetration-mode	Weld shape	Schematic	References
Partial	Bell shape: wide at the top + semi-cylindrical in depth		[26–31]
Full (wide root)	Hourglass shape: wide at the top and root + semi-cylindrical in depth		[32–37]
Full (thin root)	wide at the top + semi-cylindrical in depth + minor widening at the root		[33–35,38–40]

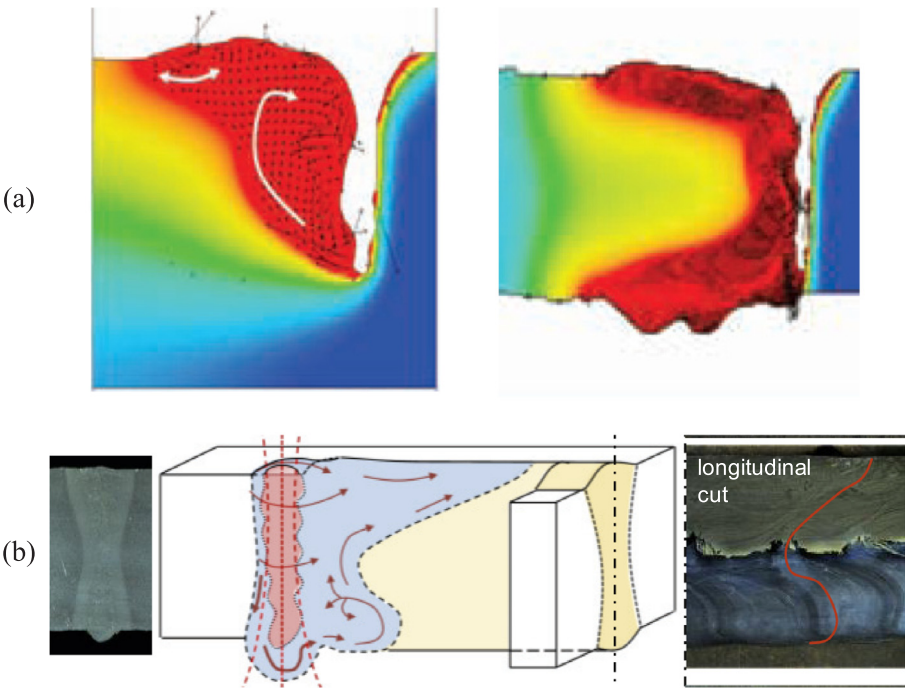


Fig. 1. (a) Melt pool geometries in the lateral weld cross section of full and partial penetration laser welding obtained by multi-physical simulation (red = melt) [41]. (b) Schematic speculation on the melt flow and the corresponding lateral and transverse cross sections of high-quality full penetration laser welding of 12 mm thick steel (red line on the longitudinal cut = solidification front shape) [45]. (For interpretation of the references to color in this figure legend, the reader is referred to the web version of this article.)

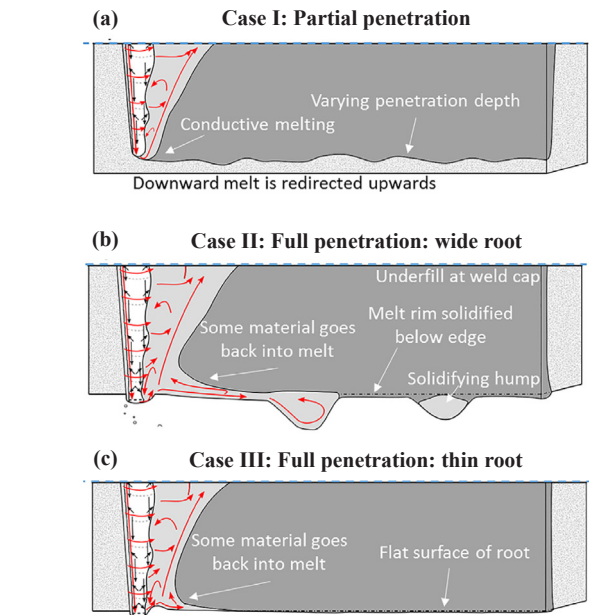


Fig. 2. Three cases of penetration-mode studied in this paper, (image modified after [48]).

Fig. 3 depicts the schematic preview of the overall experimental procedure. Steel plate of type S355J2 was used for the experiments. The chemical composition of the steel is presented in Table 3. Plates were milled to form butt joints with the dimensions depicted in Fig. 3. As shown in this figure, two blocks of the same material were tack welded

to both sides of the samples, to assure the maintenance of a zero preset gap along the I-joint seam and to limit the gap variation during welding. This also made it possible to keep the start and stop points outside the main plate. The milled surfaces were cleaned using alcohol to remove the machining liquid from the milling process.

A Trumpf TruDisk 16002 disk laser was used for the experiments, providing a maximum of 16 kW continuous-wave laser beam with a wavelength of 1030 nm and 8 mm mrad beam quality. The laser was guided through an optical fiber to a Trumpf RFO welding head with a focal length of 600 mm. The laser welding process was combined with a MAG (Metal Active Gas) welding system with a protection gas containing 92% Argon and 8% CO₂. The filler material was ESAB OK 12.50 filler wire with a diameter of 1.2 mm. The main purpose of using MAG welding was to enhance the heat balance and the process stability. Therefore, the wire feed speed or heat input of the MAG welding was relatively limited (about 10%) compared with the heat input of the laser. As depicted in Fig. 3, a laser-leading configuration was used for the welding process.

3. Experimental results

The results of experiments for Cases I and II can be seen in Figs. 4 and 5. It is evident from Fig. 4 that penetration-mode can significantly influence the heat distribution, and thereby the shape of the fusion zone. Although both experiments used the same welding parameters and heat input, they exhibited different shapes at the cross section. As shown in Fig. 4a, partial penetration welding exhibited two distinct regions at the weld cross section, namely, (i) a wide conical shape in the arc-dominated region at the top side, and (ii) a relatively narrow semi-cylindrical shape in the laser-dominated region at the root side. This is the typical weld shape for partial penetration hybrid laser welding, as

Table 2
Welding process parameters for case I and II. Notes: for case III parameters see [49], and * focal position is above the plate surface.

Laser power (kW)	Arc current (A)	Arc voltage (V)	Wire feed (m/min)	Travel speed (m/min)	Gas flow rate (l/min)	Focal position (mm)	Laser angle (degree)	Arc torch angle (degree)	Wire stickout (mm)	Arc-laser distance (mm)
12.5	84	16	2	0.9	25	25*	−7	20	15	15

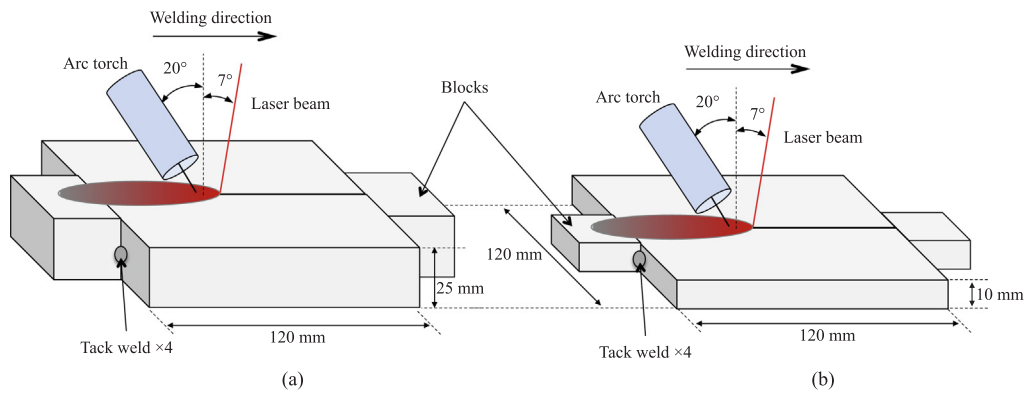


Fig. 3. Schematic of the experimental setup: (a) case I: partial penetration welding on a 25 mm plate, (b) case II: full penetration welding on a 10 mm plate, both using the same process parameters presented in Table 2. Note: the vertical axis is normal to the plate.

Table 3
Chemical composition of the steel S355J2(%) (according to the material certificate provided by the steel manufacture).

	C	Mn	P	S	Si	Cu	Al	Ni	Cr	V	Mo	CEV
S355J2	0.15	1.44	0.013	0.006	0.22	0.08	0.035	0.04	0.06	0.002	0.007	0.41

stated in Table 1. However, full penetration welding resulted in an hourglass shape, in which the weld tended to widen at the root side (Fig. 4b). As shown in Fig. 5c, the full penetration weld was associated

with minor underfilling at the top side, and two humps at the root. Consequently, the full penetration weld (Case II) fairly corresponded with the root humping regime depicted in Fig. 2b and the hourglass

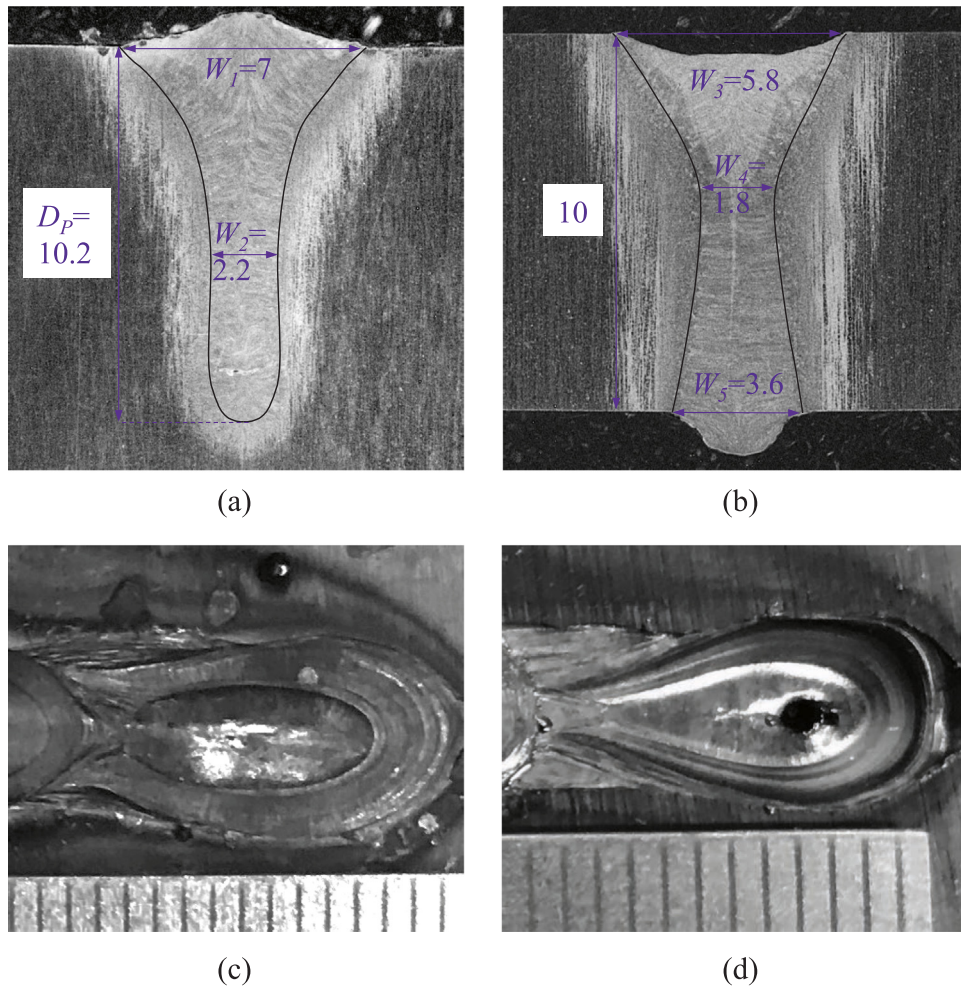


Fig. 4. Weld cross section of: (a) case I: partial penetration, (b) case II: full penetration experiments. Weld pool shape at the stop point of (a) case I: partial penetration, and (b) case II: full penetration welds. Both used the same process parameters presented in Table 2. Note: W : Width, and D_p : Penetration depth are in mm.

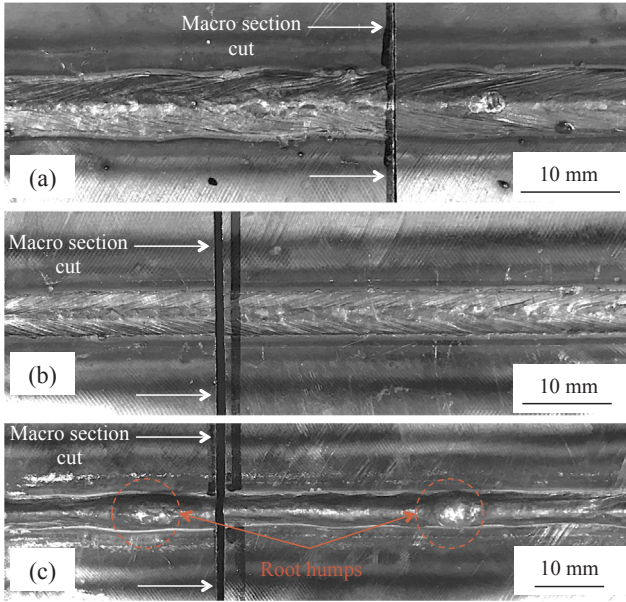


Fig. 5. Weld beads: (a) Case I: partial penetration (top side), (b) Case II: full penetration (top side), (c) Case II: full penetration (root side).

shape welds described in Table 1.

4. Finite element modeling

Hybrid laser welding was modeled using the FE method based on conductive heat transfer only. For this reason, LS-DYNA (971 R10) FE code was employed for the calculations and analysis, while pre and post processing of the model mainly used LS-PrePost (4.5).

4.1. Assumptions and exclusions

The main assumptions that were made for the modeling are as following:

- Material is isotropic and homogenous. However, some physical properties such as thermal conductivity and specific heat, are temperature dependent.
- Laser-material interaction and absorption mechanisms are neglected.
- Welding heat transfer is modeled based on only heat conduction.
- Fluid flow and convection in the melt pool is not considered. However, to compensate for the lack of fluid flow effect, an equivalent volumetric heat source with a specific shape generates the heat inside the material to obtain the fusion lines that are comparable with the experiments.
- Weld pool length can be approximated and calibrated based on the weld bead shape at the stop point of the welding experiment.
- Laser-arc distance and synergy effects are omitted.
- The zero preset gap between the plates (butt joint seam) is excluded and the FE model is treated as bead-on-plate.
- The filler material has similar material properties as the base metal.
- Surface forces, plasma pressure, shielding gas pressure, and the weld reinforcements on the top and root sides are excluded.
- The workpiece is fixed in space and the side planes of the plate parallel to the welding direction are mechanically constrained for no translation and rotation.

4.2. Thermal conduction model

The temperature distribution in the workpiece is essential in the thermal modeling of welding. In thick-section welding processes, the heat flow is three-dimensional (3D) [50]. This is essential, especially when a relatively accurate temperature distribution is required for calibration of the model with respect to the experiment in all directions. Accordingly, this study calculated the temperature distribution using the classical Fourier's heat equation for 3D transient heat conduction. This equation in a nonlinear form (temperature dependent material properties) is given by the following governing partial differential equation:

$$\rho c(T) \frac{\partial T}{\partial t} = \frac{\partial}{\partial x} \left(k(T) \frac{\partial T}{\partial x} \right) + \frac{\partial}{\partial y} \left(k(T) \frac{\partial T}{\partial y} \right) + \frac{\partial}{\partial z} \left(k(T) \frac{\partial T}{\partial z} \right) + q_v \quad (1)$$

In the above equation, q_v is the volumetric internal energy generation; T is the temperature; x , y , and z represent space coordinates; t represents time; ρ represents density; and $c(T)$ and $k(T)$ represent temperature dependent specific heat capacity and thermal conductivity, respectively.

4.3. Heat source model

As was mentioned in Section 4.1, to maintain the simplicity of the model, convective heat transfer that is induced by melt flow is excluded in this study. However, to account for the effect of melt flow, a hybrid volumetric heat source which consisted of a double-ellipsoidal heat source for the arc part and a double-conical heat source for the laser part was used. The latter is a modified version of the three-dimensional conical heat source (TDC) [17] that will be presented in this study.

4.3.1. Arc heat source

The double-ellipsoidal heat source proposed by Goldak et al. [19] can be mathematically expressed for a moving arc heat source in ξ direction, as shown in Fig. 6 using the following equation:

$$q_{af}(\xi, \psi, \zeta) = \frac{6\sqrt{3}r_f Q_a}{a_h b_h c_{hf} \pi \sqrt{\pi}} \exp\left(-\frac{3(\xi - vt)^2}{c_{hf}^2} - \frac{3\psi^2}{a_h^2} - \frac{3\zeta^2}{b_h^2}\right) \quad (2)$$

$$q_{ar}(\xi, \psi, \zeta) = \frac{6\sqrt{3}r_r Q_a}{a_h b_h c_{hr} \pi \sqrt{\pi}} \exp\left(-\frac{3(\xi - vt)^2}{c_{hr}^2} - \frac{3\psi^2}{a_h^2} - \frac{3\zeta^2}{b_h^2}\right) \quad (3)$$

In the above equations, q_{af} and q_{ar} are the volumetric heat flux at front and rear ellipsoids, respectively; v is the welding travel speed; a_h , b_h , c_{hf} , and c_{hr} are the ellipsoidal heat source parameters as in Fig. 6; r_f and r_r are the proportion coefficients at front and rear ellipsoids, respectively ($r_f + r_r = 2$); and Q_a is the effective arc power that is calculated using the following equation:

$$Q_a = \eta_a P_a = \eta_a IU \quad (4)$$

where P_a is the arc power; I represents the arc current; U represents the arc voltage; and η_a is the arc heat efficiency which was set to 70% for gas metal arc welding of S355 steel according to [51,52]. The double-ellipsoidal heat source is defined through six arbitrary parameters which must be manipulated for the calibration of the model according to the welding conditions.

4.3.2. Laser heat source

The TDC heat source model proposed by Wu et al. [17] can be mathematically expressed for a moving laser heat source in x direction as following:

$$q_l(x, y, z) = \frac{9Q_l e^3}{\pi(e^3 - 1)(z_t - z_i)(r_i^2 + r_t r_i + r_i^2)} \exp\left(-\frac{3[(x - vt)^2 + y^2]}{r_0^2}\right) \quad (5)$$

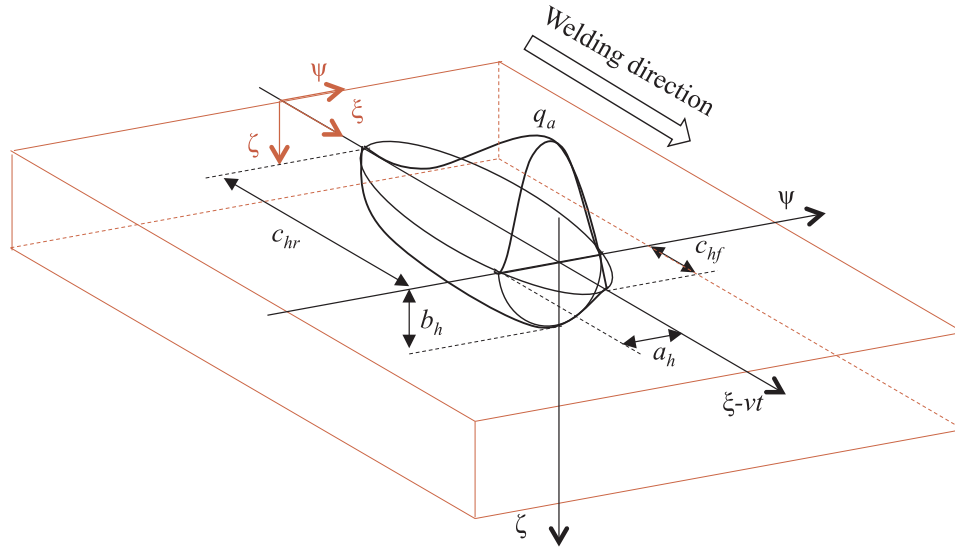


Fig. 6. Volumetric double-ellipsoidal heat source used in the hybrid heat source for modeling the arc (modified after [19]).

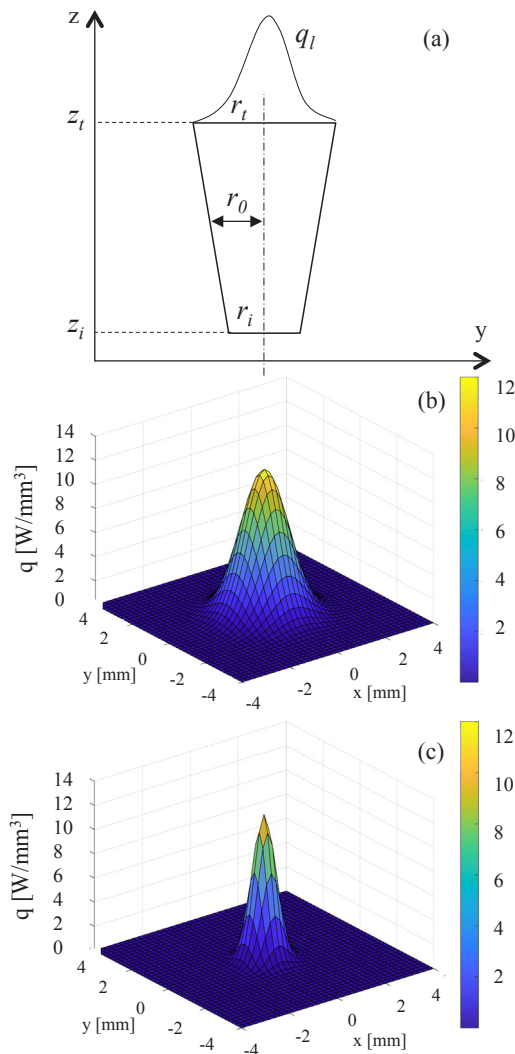


Fig. 7. (a) Schematic of TDC heat source based on [17], and heat intensity distribution at (b) the top surface (larger diameter, r_t) and (c) the bottom surface (smaller diameter, r_i). Heat source parameters: $P = 14$ kW, $\eta_l = 1$, $z_t = 25$ mm, $z_i = 0$, $r_t = 2$ mm, $r_i = 1$ mm.

where q_l is the laser heat flux; z_t , z_i , r_t , and r_i represent the z -coordinates and radii of the top and bottom surfaces, respectively (see Fig. 7a); e is the base of natural logarithm; r_0 is the distribution parameter that is linearly decreased from the top to the bottom surfaces of the conical region; and Q_l represents the effective laser power. The two latter parameters can be expressed as following:

$$r_0(z) = r_t - (r_t - r_i) \frac{z_t - z}{z_t - z_i} \quad (6)$$

$$Q_l = \eta_l P_l \quad (7)$$

where P_l is the laser power and η_l is the laser heat efficiency. The latter was set to 75% for laser welding of thick-section S355 steel with solid-state lasers and milled edge plates according to [53].

As shown in Fig. 7a and explained in [17], along the thickness of the workpiece, the diameter of the heat density distribution region is linearly decreased, depending on the radii of the top and bottom surfaces. It should be noted that, at any plane perpendicular to z -axis, the heat intensity is distributed in a Gaussian form. However, the heat density at the central axis (z -direction) is kept constant. This has been shown in Fig. 7b and c, where the heat distribution has been compared in two z -plane sections of the top and bottom surfaces.

Nevertheless, the TDC heat source – in its original form – is not capable of modeling the full penetration welds that are associated with the root widening phenomenon. For this reason, a double-conical heat source model was developed that consists of two TDC heat sources, in which the distribution factor of the lower cone can be optimized to obtain an hourglass shape distribution by a reverse cone configuration (see Fig. 9a) or a direct cone configuration (see Fig. 9b). The double-conical heat source can be mathematically expressed for a moving laser heat source in x direction, as shown in Fig. 8, using the following equations:

$$q_{l1}(x, y, z) = \frac{9Q_{l1}e^3}{\pi(e^3 - 1)(z_t - z_b)(r_i^2 + r_i r_b + r_b^2)} \exp\left(-\frac{3[(x - vt)^2 + y^2]}{r_i^2}\right) \quad (8)$$

$$q_{l2}(x, y, z) = \frac{9Q_{l2}e^3}{\pi(e^3 - 1)(z_t - z_i)(r_i^2 + r_i r_i + r_i^2)} \exp\left(-\frac{3[(x - vt)^2 + y^2]}{r_i^2}\right) \quad (9)$$

where:

$$r_1(z) = r_i - (r_i - r_b) \frac{z_t - z}{z_t - z_b} \quad (10)$$

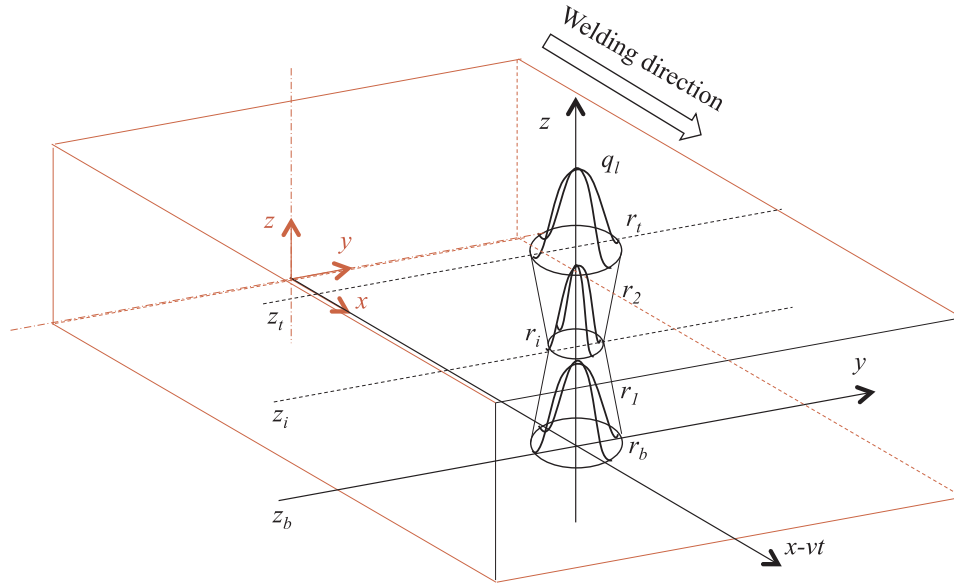


Fig. 8. Volumetric double-conical heat source with reverse cone configuration (as an example) used in the hybrid heat source for modeling the laser.

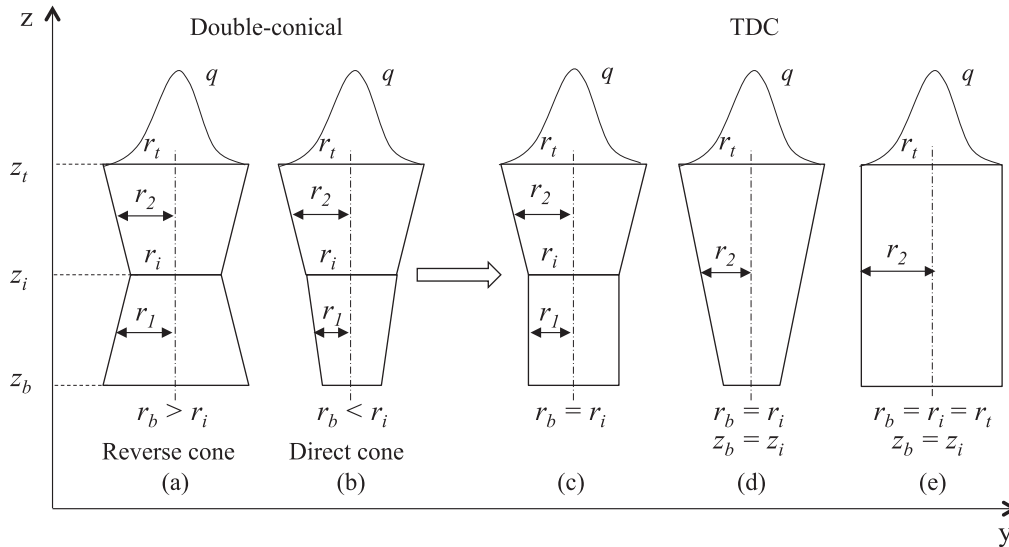


Fig. 9. Schematic of double-conical heat source with reverse and direct cone configurations and its simplified versions.

$$r_2(z) = r_t - (r_t - r_i) \frac{z_t - z}{z_t - z_i} \quad (11)$$

$$Q_{l1} = \frac{z_i - z_b}{z_t - z_b} Q_l \quad (12)$$

$$Q_{l2} = \frac{z_t - z_i}{z_t - z_b} Q_l \quad (13)$$

In the above equations, q_{l1} and q_{l2} are the laser heat flux for the lower and upper cones, respectively; z_t , z_i , z_b , r_t , r_i , and r_b represent the z -coordinates and radii of the cones, respectively; r_1 and r_2 are the distribution parameters that are linearly increased or decreased depending on the corresponding radii of the conical regions; and finally Q_{l1} and Q_{l2} represent the effective laser power for the lower and upper cones, respectively.

As shown in Fig. 9, manipulating the parameters of double-conical heat source provides different configurations including the original TDC as well. The high flexibility of this heat source potentially allows the modeling of a wide range of possible weld geometries obtained by deep

penetration keyhole welding processes.

4.3.3. Adaptive hybrid heat source

The hybrid heat source was formed by the combination of the arc and laser heat source models. However, the hybrid model is not simply the addition of the two models, due to the complex physical synergy of the arc and laser in hybrid laser welding [54].

Accordingly, in this study an adaptive heat source model was implemented to allow more flexibility in the calibration. For this reason, it was assumed that the total effective power of hybrid laser welding (Q_t) is equal to the summation of the effective power of both heat source models. Based on this assumption, the heat proportion of each heat source model was approximated so that the following condition was satisfied:

$$Q_t = \beta_a Q_a + \beta_l Q_l \quad (14)$$

where β_a and β_l are the heat partition factors for the arc and laser heat sources, respectively. This has also been done by another study on the

modeling of plasma arc welding [15]. These factors, together with the geometrical parameters of each heat source could be manipulated for the calibration of the hybrid heat source model with respect to the experimental observations. The overall mathematical equation for the moving hybrid heat source ($q_v = q_{af} + q_{ar} + q_{l1} + q_{l2}$) in xyz coordinate (as in Fig. 8) and with the consideration of the β factors can be written as below:

$$q_v = \begin{cases} \frac{6\sqrt{3}r_f\beta_a Q_a}{a_h b_h c_{hf} \pi \sqrt{\pi}} \exp\left(-\frac{3(x-vt)^2}{c_{hf}^2} - \frac{3y^2}{a_h^2} - \frac{3(z-D)^2}{b_h^2}\right); & \text{Front ellipsoid} \\ \frac{6\sqrt{3}r_r\beta_a Q_a}{a_h b_h c_{hr} \pi \sqrt{\pi}} \exp\left(-\frac{3(x-vt)^2}{c_{hr}^2} - \frac{3y^2}{a_h^2} - \frac{3(z-D)^2}{b_h^2}\right); & \text{Rear ellipsoid} \\ \frac{9\beta_l Q_{l1} e^3}{\pi(e^3-1)(z_l-z_b)(r_l^2+r_l r_b+r_b^2)} \exp\left(-\frac{3[(x-vt)^2+y^2]}{r_l^2}\right); & \text{Lower cone} \\ \frac{9\beta_l Q_{l2} e^3}{\pi(e^3-1)(z_l-z_d)(r_l^2+r_l r_d+r_d^2)} \exp\left(-\frac{3[(x-vt)^2+y^2]}{r_d^2}\right); & \text{Upper cone} \end{cases} \quad (15)$$

In the above equation, q_v is the total heat flux of the welding process and D is the plate thickness, which was used for transferring ζ to z coordinate. The moving hybrid heat source was applied as heat flux in LS-DYNA by defining a user subroutine in the LOAD_HEAT_GENERATION keyword and used for modeling the hybrid laser welding process in this study.

4.4. Thermal boundary conditions

The general solution for Eq. (1) requires initial and boundary conditions. Therefore, initial temperature was set to ambient temperature (T_0) as 293 K as following:

$$T(x, y, z, 0) = T_0(x, y, z) \quad (16)$$

Besides considering the moving heat source within the volumetric boundary, heat losses due to convection and radiation were applied to all the free surface boundaries of the 3D model. Heat loss due to convection (q_c) was taken into account using Newton's law with constant convective coefficient (h) as follows:

$$q_c = -h(T - T_0) \quad (17)$$

Similarly, heat loss due to radiation (q_r) was applied using the Stefan-Boltzman law:

$$q_r = -\sigma \epsilon (T^4 - T_0^4) \quad (18)$$

where σ is the Stefan-Boltzman constant, and ϵ is the emissivity. The values for emissivity and convective coefficient were chosen from experimental measurements for mild steel [55].

4.5. Material model

Thermo-physical properties of the steel, such as thermal conductivity, and heat capacity, as well as material's density, have significant influences on the results of welding simulations [12]. In this study, thermal conductivity and heat capacity have been considered to be temperature dependent, as shown in Fig. 10, and their values above the melting point were assumed to be constant and equal to their melting points corresponding value.

As shown in Fig. 10, the solid-state phase change has been approximated by increasing the heat capacity in the temperature intervals between 873 K to 1173 K [56]. This has also been previously done in other welding simulations, e.g. [12,55,57], on mild steels. Moreover, thermal conductivity was set to increase when the metal reaches the melting point. This enhances the heat dissipation in the melt pool and helps to obtain realistic peak temperatures [10,19,55,57]. Similarly, the specific heat capacity was enhanced during the phase change between the solid and liquid temperatures to account for the latent heat of

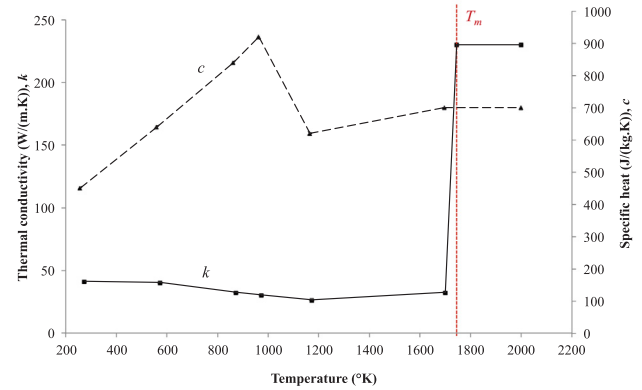


Fig. 10. Temperature dependent thermal conductivity and heat capacity; Adapted from [57,12], respectively. T_m denotes melting point.

fusion, as follows:

$$c(T) = m \left[1 - \cos 2\pi \left(\frac{T - T_S}{T_L - T_S} \right) \right], \quad T_S < T < T_L \quad (19)$$

where T_L and T_S are the liquidus and solidus temperatures, respectively, m is a multiplier that is defined in LS-DYNA such that:

$$L_f = \int_{T_S}^{T_L} c(T) dT \quad (20)$$

where L_f is the latent heat of fusion, for which its value, together with the values of T_L and T_S , were chosen for S355 steel according to [58]. Table 4 summarizes the physical properties used for the calculation.

Density value was set to 7840 kg/m³ for solid-state steel at room temperature. The material was modeled in LS-DYNA using the MAT_THERMAL_ISOTROPIC_PHASE_CHANGE keyword.

4.6. Numerical model

Full-size specimens (120 mm × 120 mm) were used for the FE models of both full and partial penetration welding. However, to save computational time, 18 mm thick plates (instead of 25 mm) were used for the partial penetration welding model. Although, due to symmetry, considering one half of the workpiece may be more convenient and economic for simulation, the calculation domain was still considered to be the whole workpiece in this study because it could be used to calculate unsymmetrical groove geometries in the future.

Three-dimensional solid elements with eight point quadrature integration were used for the model. The element sizes were determined by adjusting the resolution and accuracy of the temperature distribution in the regions of severe thermal gradients. Figs. 11 and 12 show the

Table 4
Physical properties used for the calculation.

Nomenclature	Symbol	Magnitude
Density	ρ	7840 kg/m ³
Ambient temperature	T_0	293 K
Solidus temperature	T_S	1745 K
Liquidus temperature	T_L	1810 K
Latent heat of fusion	L_f	270 kJ/kg
Convective coefficient	h	20 W/m ² K
Stefan-Boltzman constant	σ	5.67×10^{-8} W/m ² K ⁴
Emissivity	ϵ	0.9
Specific heat capacity	$c(T)$	see Fig. 10
Thermal conductivity	$k(T)$	see Fig. 10

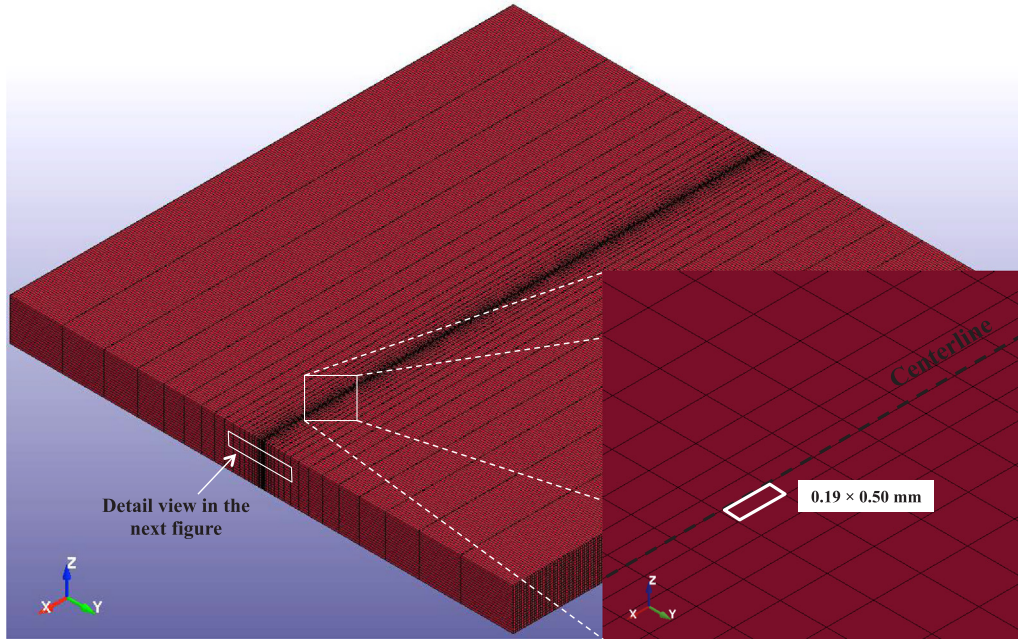


Fig. 11. FE model for a 120 mm × 120 mm × 10 mm plate and the detail views of the mesh. Note the higher densities along the welding path in the center.



Fig. 12. Detail view of the mesh in the transverse cross section (refer to Fig. 11).

mesh characteristics of the entire model. As can be seen, the density of the elements is higher in the centerline region along the welding path. The elements were generated using LS-Ingrid (3.5B), which is a pre-processor and three-dimensional mesh generator.

The solver used an implicit time integration method for the transient analysis. However, it is important to notice that the accuracy of a transient model depends on the proper selection of the time step size in accordance with the element size. In regions of severe thermal gradients during a transient analysis, the relationship between the element size in the direction of the heat flow and the time step becomes crucial [59]. This situation is inevitable in the case of our model e.g. on the fusion line where the solid material is in the vicinity of the high intensity laser heat source. For this reason, based on the element size Δs in the fine mesh region, the following condition was taken into account, to ensure the minimum time step Δt would not exceed the critical value:

$$\Delta t = \frac{(\Delta s)^2}{4\lambda} \quad (21)$$

where

$$\lambda = \frac{k}{c\rho} \quad (22)$$

In the above equations, λ is the thermal diffusivity which is dependent on the thermo-physical properties of the material. The most conservative time step could be determined when using thermal diffusivity at the melting temperature ($4.2 \times 10^{-5} \text{ m}^2/\text{s}$). Substituting this value in Eq. (21) suggests the time step $\Delta t = 2.4 \times 10^{-4} \text{ s}$ for the smallest dimension of the element size $\Delta s = 0.19 \text{ mm}$ in the vicinity of the centerline. This time step was used for the entire numerical calculation accordingly.

4.7. Validation

According to Oberkampf and Trucano [60], validation is the process where the accuracy of the model is evaluated by comparison with experimental results. It is worth noting that the same measurements cannot be used for both calibration and validation purposes [4].

In this study, the model was validated according to the experimental measurements of transient temperature for arc welding performed by Nguyen et al. [61]. The measurements were carried out on the weld toe of a bead-on-plate experiment on a 240 mm × 240 mm × 20 mm plate. The material used for the experiment was HT-780 steel, and the temperature measurement was performed by placing a thermocouple through a 16 mm hole that was positioned below the melt pool in the

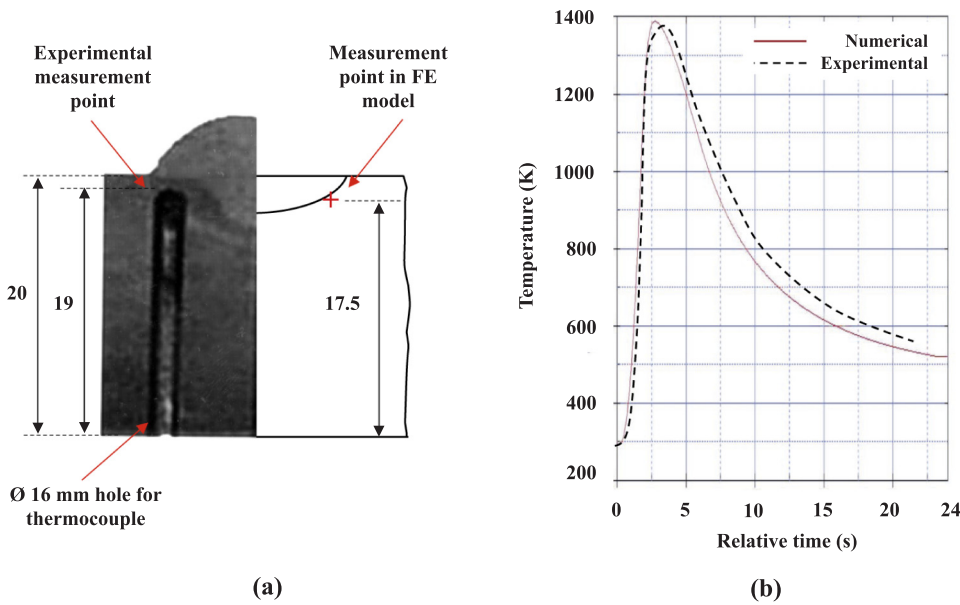


Fig. 13. Validation of the model: (a) Measurement points on the experimental sample in [61] and the FE model in this study, (b) comparison of transient temperature in the FE model with the experimental measurements replotted from [61]. Note: time axis in the plot denotes relative time, meaning that 0 s is the time that the moving heat source reaches the measurement point.

vicinity of the weld toe (see Fig. 13a). To allow comparison, the experiment in [61] was modeled using exactly the same material properties, process parameters, and double-ellipsoidal heat source parameters that Nguyen et al. suggested in their study (Table 5). The result of validation has been shown in Fig. 13. According to the figure a very good agreement can be seen between the FE model results and the measured transient temperatures.

4.8. Calibration

The model was calibrated for the three cases separately. For this reason, the hybrid heat source parameters were manipulated to obtain the weld pool shape for each experiment. Unfortunately, for Case II, it was not possible to calibrate the weld pool length at the root side, as its shape was not visible (due to the resolidified backward flows). Similarly, for Case III, the calibration of the weld pool length was omitted due to a lack of information from the source paper [49]. Moreover, for Case III, the thermo-physical material properties of Domex 420 MC steel was assumed to be the same as S355J2 steel. The parameters used for the calibration have been stated in Table 6. The fusion line was assumed to correspond with the solidus temperature $T_s = 1745$ K.

5. Results of numerical analysis

Figs. 14 and 15 compare the results of calibrated models with the experiments. The exact dimensions of the melt pools can be seen in Table 7. The results shown in Figs. 14 and 15 and Table 7 are evidence that the numerical model was in fairly good agreement with the experiments.

The double-conical heat source used in the hybrid heat source is capable of successfully modeling the three cases. In the case of the full penetration welds shown in Figs. 14b and c, employing a reverse cone configuration (as in Fig. 9a) allowed the model to account for the convective melt flow at the root side. For the partial penetration weld shown in Fig. 14a, however, the typical cone and cylinder configuration was employed that was simply obtained by applying the $r_b = r_i$ condition on the double-conical heat source (Fig. 9c). It is worth noting that the best fit for the Case I could have been obtained by applying a slightly longer (in depth) heat source (e.g. $z_r - z_b = 10.5$ mm) to decrease

Table 5

Properties and parameters used for the validation based on [61].

Symbol	Magnitude	Symbol	Magnitude
a_h	10 mm	ρ	7820 kg/m ³
b_h	2 mm	c	600 J/kg/K
c_{hf}	10 mm	k	29 W/m/K
c_{hr}	20 mm	I	230 A
r_f	1.5	U	26 V
r_r	0.5	v	0.3 m/min
η_a	0.85	λ	6.181×10^{-6} m ² /s

Table 6

Parameters used for the calibration.

Symbol	Case I Magnitude	Case II Magnitude	Case III Magnitude
v [m/min]	0.9	0.9	2.5
P_a [kW]	1.35	1.35	5
η_a	0.70	0.70	0.70
β_a	2.4	1.68	1
a_h [mm]	7	10	5
b_h [mm]	1	3	2
c_{hf} [mm]	3	3	3
c_{hr} [mm]	8	8	7
r_f	0.5	0.4	0.4
r_r	1.5	1.6	1.6
P_l [kW]	12.5	12.5	7
η_l	0.75	0.75	0.85
β_l	0.86	0.93	1
z_r [mm]	18	10	7
z_i [mm]	13	6	0.8
z_b [mm]	8	0	0
r_t [mm]	2	2.1	0.7
r_i [mm]	1.4	0.4	0.6
r_b [mm]	1.4	0.6	1.1

and increase the W_2 and the D_p dimensions, respectively. However, for simplicity, the length $z_r - z_b$ was kept at 10 mm for both Cases I and II.

Fig. 16 shows the melt pool shapes in the lateral section during welding. Fig. 17 also shows the melt profiles in the isometric view. The results are well in agreement with the schematic illustrations of the three regimes in Fig. 2. The dashed lines in Fig. 16 denote the isotherm

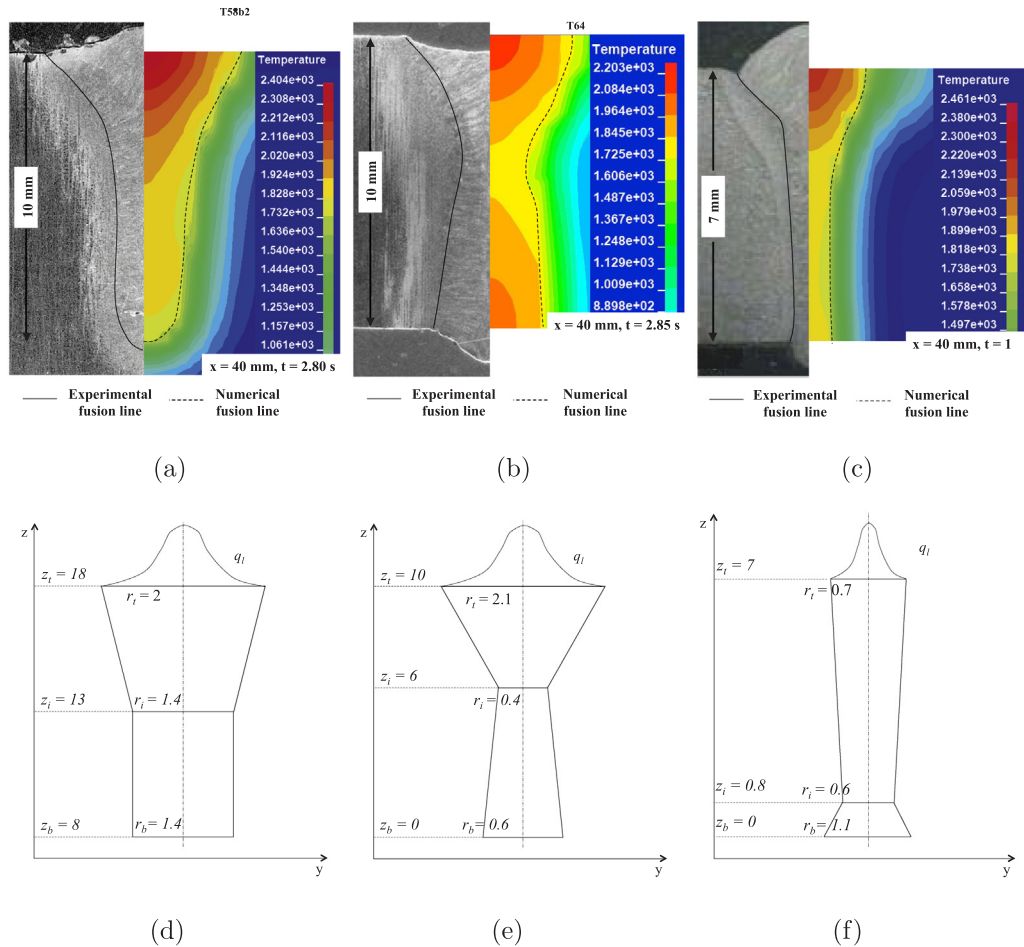


Fig. 14. Comparison of experimental and numerical weld cross sections: (a) case I: partial penetration, (b) case II: full penetration, (c) case III: full penetration, and (d-f) the schematic of their double-conical heat source geometry, respectively (The macrosection in (c) is from [49]).

that corresponds to the solidus temperature or the solidification front along the weld centerline. Comparing Cases I and II that used the same welding heat input, the melt pool shapes and the solidification front geometries were different depending on the penetration-mode. This is evidence that thermal cycles and heat distribution can be significantly different in full and partial penetration hybrid laser welding. As shown in Figs. 16 and 17, the extension of the melt at the root could be modeled in both wide root (Case II) and thin root (Case III) full penetration welding. As far as the melt pool shape or the melting point isotherms are concerned, this model – without the need for complicated fluid flow simulations – can be used for calculating temperature fields with a fairly appropriate accuracy.

6. Discussion

The model presented in this paper can be potentially employed as the basis for different metallurgical analysis and predicting micro-structural properties or calculating residual stresses in a welded component. In this section two examples of metallurgical and structural applications are discussed.

From a metallurgical point of view, for instance, comparing the distance between the isotherms in Fig. 16 (a) and (b) shows a tendency

for higher temperature gradients in partial penetration welding, especially in the root side where a considerable portion of the keyhole energy is dissipated into the solid metal below the melt. Temperature gradient is one of the most important parameters that influences the solidification mode in metal alloys [62]. It would be interesting to study the influence of penetration-mode on the temperature gradients of liquid at the solidification front, and hence, to investigate the solidification mode that can be different in some cases of full penetration welds as reported in the literature [37,63]. Further analysis is required and the authors of this paper are currently investigating the subject.

From a structural point of view, one of the main applications of thermo-mechanical models that has been widely used in industry is the computation of residual stresses induced by welding process [2]. Using the thermal analysis presented in this study, it is possible to solve the model for residual stresses that are developed after the welding process. For example, applying the mechanical boundary conditions mentioned in Section 4.1, stress analysis was performed using an elasto-plastic material model and an implicit structural stress solver in LS-DYNA that was coupled with the thermal solver. Temperature dependent mechanical properties were adopted from an external study for SM490 structural steel [64]. The results showed that the magnitude of maximum von Mises stress did not exceed 340 MPa in both full and partial

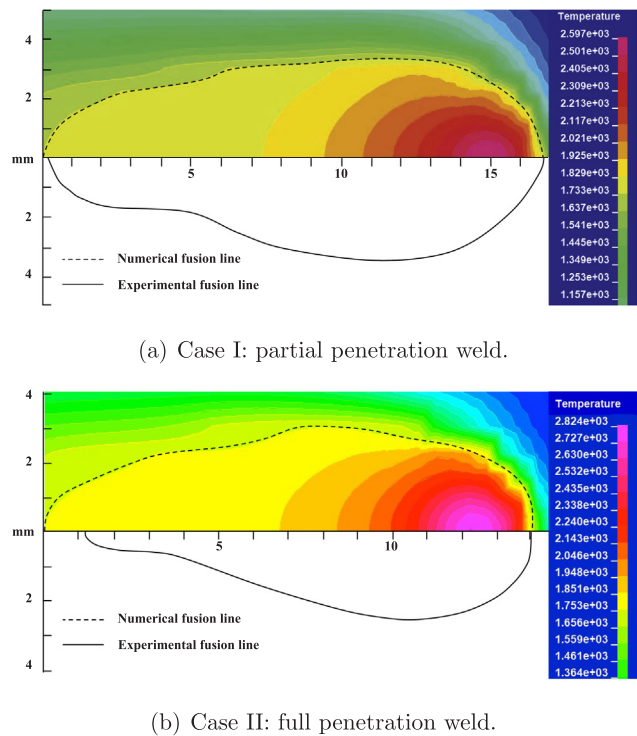


Fig. 15. Comparison of experimental and numerical melt pools on the top side, along the welding direction. The last 2 mm length of the experimental melt pool tails were approximated according to Fig. 4c and d.

penetration welds. Moreover, Figs. 18 and 19 show the results of stress analysis in longitudinal and transverse direction respectively. In welding direction, tensile residual stresses as high as the yield strength were developed in the depth of the welds and also in the heat affected zone. However, the peak tensile stresses were larger in the case of partial penetration weld. Transverse residual stresses, as shown in Fig. 19, also exhibited a relatively similar distribution in the depth and top surfaces of both full and partial penetration welds, although the residual stress at the weld toe of the partial penetration weld was less crucial compared with the full penetration weld. In addition, one should also notice that the magnitude of transverse stresses was generally lower compared with longitudinal stresses.

Apart from studying the effect of penetration-mode on the residual stresses, the numerical model presented in this study can be used for optimizing the welding process parameters and the heat input in order

to minimize residual stresses in the critical area of welded components.

In this study, experimental measurements were not carried out to verify the numerical stress analysis, as the subject was not the main aim of this paper. However, in general, the results reflect similar tendency in stress distribution compared with other studies in the literature [10,65]. For example, considering the residual stresses on a transverse line on the top surface of the sections shown in Fig. 18, longitudinal stress magnitude has a slight raise from the weld to the heat affected zone and then is decreased to compressive stresses as moving away from the weld in about 15 mm distance from the weld centerline. Similarly, considering the residual stresses on the same top surface line in Fig. 19, the transverse stress magnitudes are minimal on the weld surface and are decreased again after a sharp raise in a region about 15 mm far from the weld centerline. This may be counted as an indication for the validity of the results as the same tendencies have been reported in the above-mentioned references. Nevertheless, experimental validation is necessary as welding parameters, mechanical boundary conditions, and material properties and dimensions are often unique in each study, which makes such indirect validations and comparisons difficult. Accordingly, further analysis is required and the subject is currently under investigation by the authors.

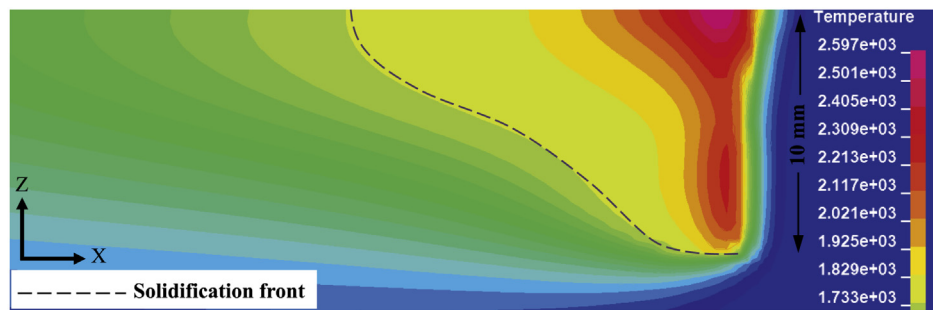
7. Conclusions

Hybrid laser welding was performed for full and partial penetration modes on butt joints of structural steel. A numerical model using 3D transient FE analysis and thermal conduction heat transfer was presented for calculating the temperature fields. An adaptive hybrid heat source was employed for this purpose. A double-conical heat source was developed based on the TDC heat source in the literature. The model was validated and calibrated with various experiments. The following conclusions can be drawn according to the results of study:

- The double-conical heat source allowed the modeling of three common weld transverse cross section geometries that are obtained by hybrid laser welding of thick-section steel: (i) partial penetration welding: *bell shape*, (ii) full penetration welding with major root widening: *hourglass shape*, and (iii) full penetration welding with minor root widening.
- For a given welding process parameters for 10 mm penetration depth, partial penetration welding exhibited a bell shape weld cross section, whereas full penetration welding resulted in an hourglass shape weld cross section. Full penetration weld was associated with the extension of the melt at the root. This is evidence that thermal cycles and heat distribution could be significantly different in full and partial penetration hybrid laser welding, despite the fact that the same welding heat input was employed.

Table 7
Comparison of experimental and numerical melt pool dimensions (in mm). Note: Experimental results for case I and II are the average of two macrosection measurements. L denotes the melt pool length along the welding direction.

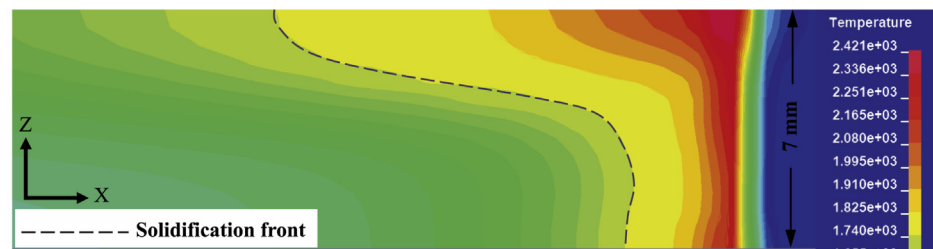
	Case I (Partial pen.)					Case II (Full pen.)					Case III (Full pen.)				
	W_1	W_2	D_p	L_{top}	L_{root}	W_3	W_4	W_5	L_{top}	L_{root}	W_{top}	W_{middle}	W_{root}	L_{top}	L_{root}
Experimental	7	2.2	10.2	16.5	–	5.8	1.8	3.6	12.9	N/A	3.5	0.8	1.0	N/A	N/A
Numerical	6.4	3.2	9.8	16.8	–	5.5	2.3	3.6	14	10.5	3.5	1	1.1	14	3.5



(a) Case I: partial penetration ($P_l=12$ kW, $P_a=1.35$ kW, $v=0.9$ m/min).



(b) Case II: full penetration: wide root ($P_l=12$ kW, $P_a=1.35$ kW, $v=0.9$ m/min).



(c) Case III: full penetration: thin root ($P_l=7$ kW, $P_a=5$ kW, $v=2.5$ m/min).

Fig. 16. Lateral (longitudinal) section on the centerline of the welds (parameters of the heat source models are in Table 6).

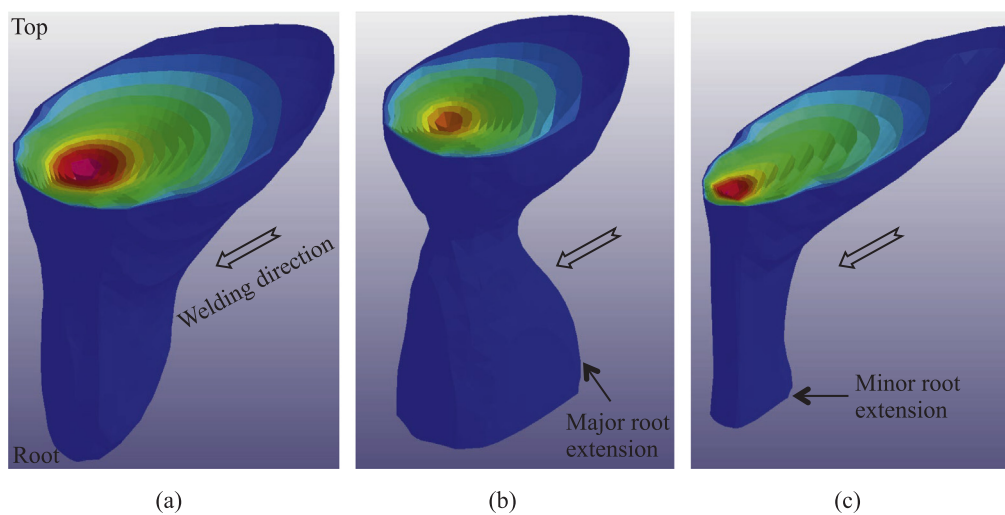


Fig. 17. Isometric view of the melt profiles: (a) Case I, (b) Case II, and (c) Case III.

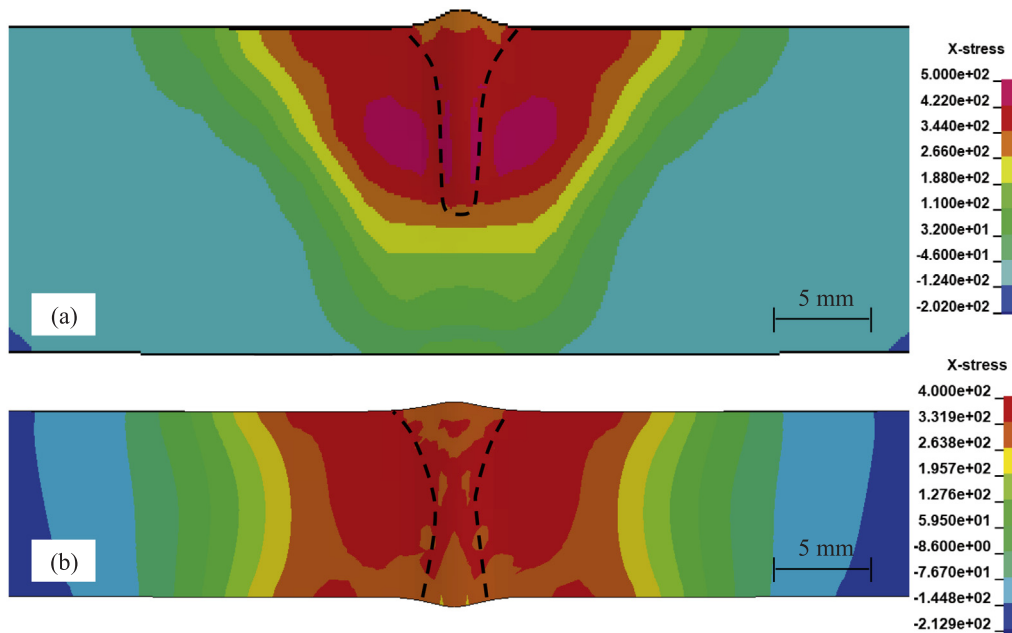


Fig. 18. Residual stresses in welding direction in the middle of the plate after 600 s: (a) Case I, (b) Case II. Note: units are in MPa.

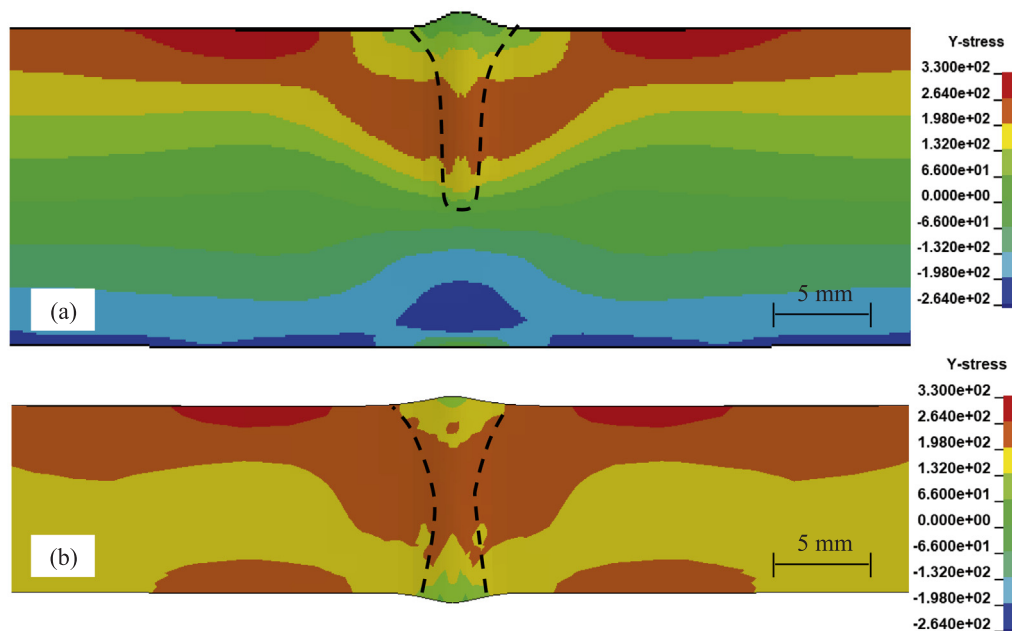


Fig. 19. Transverse residual stresses in the middle of the plate after 600 s: (a) Case I, (b) Case II. Note: units are in MPa.

Acknowledgement

This study was supported in part by the Danish National Advanced Technology Foundation, project: *Cost-Effective Mass Production of Universal Foundations for Large Offshore Wind Parks*. In addition, the authors would like to thank Force Technology for providing welding and radiographic examination facilities.

References

- [1] Z.H. Rao, S.M. Liao, H.L. Tsai, Modelling of hybrid laser-GMA welding: review and challenges, *Sci. Technol. Weld. Joining* 16 (4) (2011) 300–305, <https://doi.org/10.1179/1362171811y.0000000022>.
- [2] M. Dal, R. Fabbro, An overview of the state of art in laser welding simulation, *Opt. Laser Technol.* 78 (2016) 2–14, <https://doi.org/10.1016/j.optlastec.2015.09.015> (INVITED).
- [3] A.P. Mackwood, R.C. Crafer, Thermal modelling of laser welding and related processes: a literature review, *Opt. Laser Technol.* 37 (2) (2005) 99–115, <https://doi.org/10.1016/j.optlastec.2005.09.015>.

- org/10.1016/j.optlastec.2004.02.017.
- [4] L.E. Lindgren, Numerical modelling of welding, *Comput. Methods Appl. Mech. Eng.* 195 (48–49) (2006) 6710–6736, <https://doi.org/10.1016/j.cma.2005.08.018>.
 - [5] J. Svenungsson, I. Choquet, A.F. Kaplan, Laser welding process – a review of keyhole welding modelling, *Phys. Procedia* 78 (August) (2015) 182–191, <https://doi.org/10.1016/j.phpro.2015.11.042>.
 - [6] J. Dowden (Ed.), *The Theory of Laser Materials Processing: Heat and Mass Transfer in Modern Technology*, second ed., Springer Series in Materials Science, 2017.
 - [7] A. Otto, M. Schmidt, Towards a universal numerical simulation model for laser material processing, *Phys. Procedia* 5 (2010) 35–46, <https://doi.org/10.1016/j.phpro.2010.08.120> URL <<http://linkinghub.elsevier.com/retrieve/pii/S1875389210005468>> .
 - [8] A. Otto, H. Koch, R.G. Vazquez, Multiphysical simulation of laser material processing, *Phys. Procedia* 39 (2012) 843–852, <https://doi.org/10.1016/j.phpro.2012.10.109>.
 - [9] W.I. Cho, S.J. Na, C. Thomy, F. Vollertsen, Numerical simulation of molten pool dynamics in high power disk laser welding, *J. Mater. Process. Technol.* 212 (1) (2012) 262–275, <https://doi.org/10.1016/j.jmatprotec.2011.09.011>.
 - [10] D. Deng, FEM prediction of welding residual stress and distortion in carbon steel considering phase transformation effects, *Mater. Des.* 30 (2) (2009) 359–366, <https://doi.org/10.1016/j.matdes.2008.04.052>.
 - [11] I. Sattari-Far, M.R. Farahani, Effect of the weld groove shape and pass number on residual stresses in butt-welded pipes, *Int. J. Press. Vessels Pip.* 86 (11) (2009) 723–731, <https://doi.org/10.1016/j.ijpvp.2009.07.007>.
 - [12] A.A. Bhatti, Z. Barsoum, H. Murakawa, I. Barsoum, Influence of thermo-mechanical material properties of different steel grades on welding residual stresses and angular distortion, *Mater. Des.* 65 (2015) 878–889, <https://doi.org/10.1016/j.matdes.2014.10.019>.
 - [13] M. Zain-ul Abdein, D. Nelias, J.F. Jullien, D. Deloison, Prediction of laser beam welding-induced distortions and residual stresses by numerical simulation for aeronautic application, *J. Mater. Process. Technol.* 209 (6) (2009) 2907–2917, <https://doi.org/10.1016/j.jmatprotec.2008.06.051>.
 - [14] P. Martinson, S. Daneshpour, M. Koçak, S. Riekehr, P. Staron, Residual stress analysis of laser spot welding of steel sheets, *Mater. Des.* 30 (9) (2009) 3351–3359, <https://doi.org/10.1016/j.matdes.2009.03.041>.
 - [15] C.S. Wu, Q.X. Hu, J.Q. Gao, An adaptive heat source model for finite-element analysis of keyhole plasma arc welding, *Comput. Mater. Sci.* 46 (1) (2009) 167–172, <https://doi.org/10.1016/j.commatsci.2009.02.018>.
 - [16] I. Bendaoud, S. Mattei, E. Cicala, I. Tomashchuk, H. Andrzejewski, P. Sallamand, A. Mathieu, F. Bouchaud, The numerical simulation of heat transfer during a hybrid laser/MIG welding using equivalent heat source approach, *Opt. Laser Technol.* 56 (2014) 334–342, <https://doi.org/10.1016/j.optlastec.2013.09.007> <<http://linkinghub.elsevier.com/retrieve/pii/S0030399213003320>> .
 - [17] C. Wu, H.G. Wang, Y.M. Zhang, A new heat source model for keyhole plasma arc welding in FEM analysis of the temperature profile, *Weld. J.* 85 (12) (2006) 284–291.
 - [18] N.S. Shanmugam, G. Buvanashakaran, K. Sankaranarayanan, S. Ramesh Kumar, A transient finite element simulation of the temperature and bead profiles of T-joint laser welds, *Mater. Des.* 31 (9) (2010) 4528–4542, <https://doi.org/10.1016/j.matdes.2010.03.057>.
 - [19] J. Goldak, A. Chakravarti, M. Bibby, A new finite element model for welding heat sources, *Metall. Trans. B* 15 (2) (1984) 299–305.
 - [20] J. Goldak, M. Bibby, J. Moore, R. House, B. Patel, Computer modeling of heat flow in welds, *Metall. Trans. B* 17B (September) (1986) 587–600.
 - [21] T.F. Flint, J.A. Francis, M.C. Smith, J. Balakrishnan, Extension of the double-ellipsoidal heat source model to narrow-groove and keyhole weld configurations, *J. Mater. Process. Technol.* 246 (2017) 123–135, <https://doi.org/10.1016/j.jmatprotec.2017.02.002>.
 - [22] E. Ranatowski, Thermal modelling of laser welding. Part I: the physical basis of laser welding, *Adv. Mater. Sci. Eng.* 3 (1) (2003) 34–40.
 - [23] J. Rahman Chukkan, M. Vasudevan, S. Muthukumar, R. Ravi Kumar, N. Chandrasekhar, Simulation of laser butt welding of AISI 316L stainless steel sheet using various heat sources and experimental validation, *J. Mater. Process. Technol.* 219 (2015) 48–59, <https://doi.org/10.1016/j.jmatprotec.2014.12.008>.
 - [24] W. Piekarska, M. Kubiak, Three-dimensional model for numerical analysis of thermal phenomena in laser-arc hybrid welding process, *Int. J. Heat Mass Transf.* 54 (23–24) (2011) 4966–4974, <https://doi.org/10.1016/j.ijheatmasstransfer.2011.07.010>.
 - [25] C. Heinze, C. Schwenk, M. Rethmeier, Effect of heat source configuration on the result quality of numerical calculation of welding-induced distortion, *Simul. Model. Pract. Theory* 20 (1) (2012) 112–123, <https://doi.org/10.1016/j.simpat.2011.09.004>.
 - [26] M.O. Gebhardt, A. Gumenyuk, M. Rethmeier, Numerical analysis of hot cracking in laser-hybrid welded tubes, *Adv. Mater. Sci. Eng.* (2013), <https://doi.org/10.1155/2013/520786>.
 - [27] O.M. Akselsen, G. Wiklund, E. Ostby, A. Sorgjard, A. Kaplan, A first assessment of laser hybrid welding of 420 mPa steel for offshore structure application. in: A.F.H. Kaplan, H. Engstrom (Eds.), 14th Nordic Laser Materials Processing Conference NOLAMP, Lulea tekniska universitet, 2013, pp. 171–182.
 - [28] G. Wiklund, O. Akselsen, A.J. Sørgerd, A.F. Kaplan, Geometrical aspects of hot cracks in laser-arc hybrid welding, *J. Laser Appl.* 26 (1) (2014) 012003.
 - [29] M. Kristiansen, F. Farrokhi, E. Kristiansen, S. Villumsen, Application of hybrid laser arc welding for the joining of large offshore steel foundations, *Phys. Procedia* 89 (2017) 197–204, <https://doi.org/10.1016/j.phpro.2017.08.018>.
 - [30] F. Farrokhi, S.E. Nielsen, R.H. Schmidt, S.S. Pedersen, M. Kristiansen, Effect of cut quality on hybrid laser arc welding of thick section steels, *Phys. Procedia* 78 (August) (2015) 65–73, <https://doi.org/10.1016/j.phpro.2015.11.018>.
 - [31] I. Bunaziv, J. Frostevar, O.M. Akselsen, A.F. Kaplan, Process stability during fiber laser-arc hybrid welding of thick steel plates, *Opt. Lasers Eng.* 102 (November 2017) (2018) 34–44, <https://doi.org/10.1016/j.optlaseng.2017.10.020>.
 - [32] U. Reisgen, S. Olschok, M. Weinbach, O. Engels, Welding of high thickness steel plates using a fiber coupled diode laser with 50 kW of output power, in: *Lasers in Manufacturing Conference (LIM)*, WLT, 2017.
 - [33] Q. Pan, M. Mizutani, Y. Kawahito, S. Katayama, High power disk laser-metal active gas arc hybrid welding of thick high tensile strength steel plates, *J. Laser Appl.* 28 (1) (2016) 012004, <https://doi.org/10.2351/1.4934939> <<http://scitation.aip.org/content/lia/journal/jla/28/1/10.2351/1.4934939>> .
 - [34] M.O. Gebhardt, A. Gumenyuk, V. Quiroz Penaranda, M. Rethmeier, Laser/GMA hybrid welding of thick-walled precision pipes, *Weld. Cutting* 5 (2012) 312–318.
 - [35] X. Cao, P. Wanjara, J. Huang, C. Munro, A. Nolting, Hybrid fiber laser – arc welding of thick section high strength low alloy steel, *Mater. Des.* 32 (6) (2011) 3399–3413, <https://doi.org/10.1016/j.matdes.2011.02.002>.
 - [36] E.W. Reutzel, M.J. Sullivan, D.A. Mikesic, Joining pipe with the hybrid laser-GMAW process: weld test results and cost analysis, *Weld. J.* (Miami, Fla) 85(6) (2006) 66–71. <<http://www.scopus.com/inward/record.url?eid=2-s2.0-33744970231&partnerID=40&md5=9115b07d542b883bb69a0786d1ce05a>> .
 - [37] F. Farrokhi, R.M. Larsen, M. Kristiansen, Single-pass hybrid laser welding of 25 mm thick steel, *Phys. Procedia* 89 (2017) 49–57, <https://doi.org/10.1016/j.phpro.2017.08.019>.
 - [38] F. Vollertsen, S. Grunenwald, M. Rethmeier, A. Gumenyuk, U. Reisgen, S. Olschok, Welding thick steel plates with fibre lasers and GMAW, *Weld. World* 54 (3–4) (2010) R62–R70, <https://doi.org/10.1007/BF03263489> <<http://link.springer.com/article/10.1007/BF03263489%5Cnhttp://link.springer.com/content/pdf/10.1007/BF03263489.pdf>> .
 - [39] M. Rethmeier, G. Sergej, L. Marco, G. Andrey, Laser-hybrid welding of thick plates up to 32 mm using a 20 kW fibre laser, *Quart. J. Jpn. Weld. Soc.* 27 (2) (2009) 74–79, <https://doi.org/10.2207/qjws.27.74s>.
 - [40] G. Li, C. Zhang, M. Gao, X. Zeng, Role of arc mode in laser-metal active gas arc hybrid welding of mild steel, *Mater. Des.* 61 (2014) 239–250, <https://doi.org/10.1016/j.matdes.2014.04.079> Available from: <9605103> .
 - [41] J. Powell, T. Ilar, J. Frostevar, M.J. Torkamany, S.-J. Na, D. Petring, L. Zhang, A.F.H. Kaplan, Weld root instabilities in fiber laser welding, *J. Laser Appl.* 27 (S2) (2015) S29008, <https://doi.org/10.2351/1.4906390> <<http://scitation.aip.org/content/lia/journal/jla/27/S2/10.2351/1.4906390>> .
 - [42] Z. Zhang, C. Wu, Effect of fluid flow in the weld pool on the numerical simulation accuracy of the thermal field in hybrid welding, *J. Manuf. Process.* 20 (2015) 215–223, <https://doi.org/10.1016/j.jmapro.2015.08.001>.
 - [43] M. Schaefer, N. Speker, R. Weber, T. Harter, T. Graf, Lasers in Manufacturing Conference 2015 Analysing Hot Crack Formation in Laser Welding of Tempered Steel, *Lasers in Manufacturing Conference*, vol. 1, 2015.
 - [44] L. Zhang, J. Zhang, A. Gumenyuk, M. Rethmeier, S. Na, Numerical simulation of full penetration laser welding of thick steel plate with high power high brightness laser, *J. Mater. Process. Technol.* 214 (8) (2014) 1710–1720, <https://doi.org/10.1016/j.jmatprotec.2014.03.016> <<http://linkinghub.elsevier.com/retrieve/pii/S092401361400096X>> .
 - [45] P. Haug, V. Rominger, N. Speker, R. Weber, T. Graf, M. Weigl, M. Schmidt, Influence of laser wavelength on melt bath dynamics and resulting seam quality at welding of thick plates, *Phys. Procedia* 41 (2013) 49–58, <https://doi.org/10.1016/j.phpro.2013.03.051>.
 - [46] H.L. Wei, J.J. Blecher, T.A. Palmer, T. DebRoy, Fusion zone microstructure and geometry in complete joint penetration laser arc hybrid welding of low alloy steel, *Weld. J.* 94 (4) (2015) 135–144s.
 - [47] LSTC, LS-DYNA keyword user's manual, vol. I, 2015.
 - [48] J. Frostevar, Factors affecting weld root morphology in laser keyhole welding, *Opt. Lasers Eng.* 101 (2018) 89–98, <https://doi.org/10.1016/j.optlaseng.2017.10.005>.
 - [49] J. Frostevar, A.F.H. Kaplan, Undercuts in laser arc hybrid welding, *Phys. Procedia* 56 (C) (2014) 663–672, <https://doi.org/10.1016/j.phpro.2014.08.071>.
 - [50] N.T. Nguyen, Y.W. Mai, S. Simpson, A. Ohta, Analytical approximate solution for double ellipsoidal heat source in finite thick plate, *Weld. J.* 83 (3) (2004) 82s–93s.
 - [51] K. Hemmes, M. Farajian, M. Boin, Numerical studies of welding residual stresses in tubular joints and experimental validations by means of x-ray and neutron diffraction analysis, *Mater. Des.* 126 (2017) 339–350, <https://doi.org/10.1016/j.matdes.2017.03.088> <<http://linkinghub.elsevier.com/retrieve/pii/S026412751730343X>> .
 - [52] J. Chen, C. Schwenk, C.S. Wu, M. Rethmeier, Predicting the influence of groove angle on heat transfer and fluid flow for new gas metal arc welding processes, *Int. J. Heat Mass Transf.* 55 (1–3) (2012) 102–111, <https://doi.org/10.1016/j.ijheatmasstransfer.2011.08.046>.
 - [53] M. Sokolov, A. Salminen, V. Somonov, A.F.H. Kaplan, Laser welding of structural steels: influence of the edge roughness level, *Opt. Laser Technol.* 44 (7) (2012) 2054–2071, <https://doi.org/10.1016/j.optlastec.2012.03.025>.
 - [54] L. Liu, Hybrid welding of magnesium alloys, in: F.O. Olsen (Ed.), *Hybrid Laser-Arc Welding*, Woodhead Publishing Limited, 2009, pp. 143–177.
 - [55] P.V. Jeberg, Automatic Process Optimised Weld Planning of Full Penetration I-joint

- GMA Welding (Ph.D. thesis), Aalborg University (AAU), 2005.
- [56] C. Vogel, C. Juhl, E. Maahn, *Metallurgi for ingeniører*, seventh ed., Akademisk Forlag, 1995.
- [57] M. Birk-Sørensen, *Simulation of Welding Distortions in Ship Section* (Ph.D. thesis), Technical University of Denmark (DTU), 1999.
- [58] E. Le Guen, M. Carin, R. Fabbro, F. Coste, P. Le Masson, 3D heat transfer model of hybrid laser Nd: Yag-MAG welding of S355 steel and experimental validation, *Int. J. Heat Mass Transf.* 54 (7–8) (2011) 1313–1322, <https://doi.org/10.1016/j.ijheatmasstransfer.2010.12.010>.
- [59] E. Stamper, Calculating Solution Settings for a Transient Thermal Analysis – Part 2, 2016. < www.caeai.com > .
- [60] W.L. Oberkampf, T.G. Trucano, Verification and validation in computational fluid dynamics, *Prog. Aerosp. Sci.* 38 (3) (2002) 209–272, [https://doi.org/10.1016/S0376-0421\(02\)00005-2](https://doi.org/10.1016/S0376-0421(02)00005-2).
- [61] N. Nguyen, A. Ohta, K. Matsuoka, N. Suzuki, Y. Maeda, Analytical solutions for transient temperature of semi-infinite body subjected to 3-D moving heat sources, *Weld. Res. Suppl. I* (August) (1999) 265–274. e:%5CBIBLIO%5CArticles%5CSolution_transient-temp-3D-moving-heat-source_Nguyen_1999.pdf.
- [62] J.C. Lippold, *Welding Metallurgy and Weldability*, John Wiley & Sons, 2015, <https://doi.org/10.1002/9781118960332>.
- [63] M. Wahba, M. Mizutani, S. Katayama, Single pass hybrid laser-arc welding of 25 mm thick square groove butt joints, *Mater. Des.* 97 (May) (2016) 1–6, <https://doi.org/10.1016/j.matdes.2016.02.041>.
- [64] K. Yuan, Y. Sumi, Simulation of residual stress and fatigue strength of welded joints under the effects of ultrasonic impact treatment (UIT), *Int. J. Fatigue* 92 (2016) 321–332, <https://doi.org/10.1016/j.ijfatigue.2016.07.018>.
- [65] Y. Ye, J. Cai, X. Jiang, D. Dai, D. Deng, Influence of groove type on welding-induced residual stress, deformation and width of sensitization region in a SUS304 steel butt welded joint, *Adv. Eng. Softw.* 86 (2015) 39–48, <https://doi.org/10.1016/j.advengsoft.2015.04.001>.